ACS EARTH AND SPACE CHEMISTRY

http://pubs.acs.org/journal/aesccq

Article

Size-Dependent Morphology, Composition, Phase State, and Water Uptake of Nascent Submicrometer Sea Spray Aerosols during a Phytoplankton Bloom

Chathuri P. Kaluarachchi, Victor W. Or, Yiling Lan, Chamika K. Madawala, Elias S. Hasenecz, Daniel R. Crocker, Clare K. Morris, Hansol D. Lee, Kathryn J. Mayer, Jonathan S. Sauer, Christopher Lee, Glorianne Dorce, Francesca Malfatti, Elizabeth A. Stone, Christopher D. Cappa, Vicki H. Grassian, Kimberly A. Prather, and Alexei V. Tivanski*

Cite This: *ACS Earth Space Chem.* 2022, 6, 116−130

Read Online

ACCESS | Metrics & More | Article Recommendations | Supporting Information

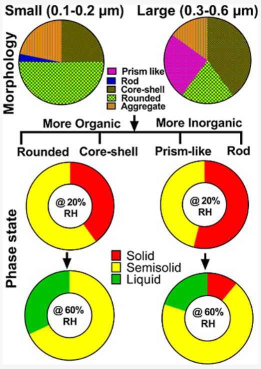

ABSTRACT: The impact of sea spray aerosols (SSAs) on Earth's climate remains uncertain in part due to size-dependent particle-to-particle variability in SSA physicochemical properties such as morphology, composition, phase state, and water uptake that can be further modulated by the environment relative humidity (RH). The current study investigates these properties as a function of particle size and RH, while focusing on submicrometer nascent SSA (0.1−0.6 μm) collected throughout a phytoplankton bloom. Filter-based thermal optical analysis, atomic force microscopy (AFM), and AFM photothermal infrared spectroscopy (AFM−PTIR) were utilized in this regard. AFM imaging at 20% RH identified five main SSA morphologies: prism-like, core−shell, rounded, rod, and aggregate. The majority of smaller SSAs throughout a bloom were rounded, while larger SSAs were core−shell. Filter-based measurements revealed an increasing organic mass fraction with decreasing SSA size. The organic matter is shown to primarily reside in a rounded and core−shell SSA, while the prism-like and rod SSA are predominantly inorganic salts (i.e., sodium chloride, nitrates, and sulfates) with relatively low organic content, as determined by AFM−PTIR spectroscopy. AFM phase state measurements at 20% RH revealed an increasing abundance of core−shell SSA with semisolid shells and rounded SSA with a solid phase state, as the particle size decreases. At 60% RH, shells of core−shell and rounded SSA uptake water, become less viscous, and their phase states change into either semisolid or liquid. Collectively, findings reveal the dynamic and size-dependent nature of SSA's morphology, composition, phase states, and water uptake, which should be considered to accurately predict their climate-related effects.

KEYWORDS: *atomic force microscopy, nascent sea spray aerosol, single particle, size-dependent, morphology, phase state, water uptake*

■ INTRODUCTION

Sea spray aerosols (SSAs) are generated upon the bursting of air bubbles entrained from breaking waves in the ocean and constitute a significant fraction of natural aerosol mass concentration in atmosphere.[1−5] SSA climate-relevant effects include their ability to influence Earth's radiative budget directly, by scattering and absorbing incoming solar radiation, and indirectly, by acting as cloud condensation nuclei (CCN) or ice nuclei (IN).[1,2,6−12] Due to their abundance, SSAs provide a significant source of suspended interfaces that can facilitate heterogeneous chemical reactions with atmospheric gases.[1,13−15] During air bubble bursting at the ocean−air interface, the organic, inorganic, and biological species that are either dissolved in bulk seawater or enriched at the sea surface microlayer (SML, the uppermost organic layer with submicrometer thickness) can be transferred into the SSA.[16−22] Hence, the chemical complexity of SSA can vary significantly depending on composition and biological activity in the seawater and SML, as well as SSA generation mechanisms via bubbles bursting.[3,16,19,20,23−27] For example, submicrometer SSAs, produced via bubble-cap bursting (i.e., film drops, typical dry SSA diameter ≤ 0.25 μm) are significantly enriched with organic matter compared to SSAs produced via bubble-cavity collapse (i.e., jet drops, typical dry SSA diameter ≥ 0.25 μm), which are predominantly inorganic salts.[3,16−19,21,24,28−30] Additionally, the type and concentration of organic molecules in SSA can vary with phytoplankton and heterotrophic bacteria (HB) activities in the seawater.[3,21,30,31]

Measurements of chemical speciation in SSAs generated under controlled laboratory and mesocosm experiments

Received: September 2, 2021
Revised: October 21, 2021
Accepted: November 16, 2021
Published: December 9, 2021

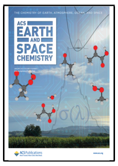

revealed the presence of organic compounds, such as alkanes, fatty acids, saccharides, proteins, and inorganic compounds containing sodium, calcium, and chloride.[1,3,16,17,20,25,30−32] This chemical complexity in SSA can govern their direct and indirect aerosol effects in atmosphere.[2,8,10,26,33−42] For example, the organic and inorganic content in SSA controls their phase state and water uptake, which alters SSA's atmospheric aging, scattering of solar radiation, CCN and IN abilities.[2−4,6,9,10,15,26,34−40,43−49] Prior studies performed on model and nascent SSA revealed the existence of different morphologies or physicochemical mixing states (core−shell, prism-like, rod, and rounded)[2,8−10,26,34,41,42,50] at varying phase states from solid to semisolid to liquid,[2,8,38,41,42] and differing extent of water uptake.[9,35,36,40] In the context of phase state, the characteristic mass-transport time for nonvolatile organic species in a semisolid particle (viscosity range of ∼10^2 to 10^{12} Pa s, particle diameter of 100 nm) can vary from seconds to years; while for a liquid particle, it only takes microseconds to milliseconds.[15,51,52] Hence, the rate of atmospheric chemical aging of semisolid SSAs is relatively lower compared to a liquid SSA.[15,52,53] Furthermore, solid SSAs are more likely to be activated as IN, while semisolid and liquid SSA are more likely to be activated as CCN.[15,44,45,54] The comprehensive information about SSA phase state and water uptake is thus important to accurately predict their climatic relevance. To our knowledge, no existing studies have directly probed and correlated the size, morphology, and seawater biological activity-dependent phase state and water uptake of submicrometer nascent SSA under subsaturated RH conditions.

Herein, we investigate these properties by focusing on nascent SSA (size range of 0.1−0.6 μm) generated throughout a phytoplankton bloom from the Sea Spray Chemistry And Particle Evolution (SeaSCAPE) mesocosm experiment, in Summer 2019.[5] The experiment was performed in a wave-simulation channel facility containing filtered seawater from the southern coast of California.[5] Filter-based thermal optical analysis was used to investigate the size-dependent bulk-ensemble organic mass fraction in SSA, which provided an ensemble-averaged value for the entire SSA population, where an organic enrichment was observed for smaller SSA. To better understand the size-dependent and particle-to-particle variability in SSA organic enrichment and their corresponding morphology, phase state, and water uptake, atomic force microscopy (AFM) and AFM photothermal infrared spectroscopy (AFM−PTIR) analysis were employed. A significant variability of these physicochemical properties was observed, highlighting the need to consider it in future studies to accurately predict SSA's climate-related effects.

■ MATERIALS AND METHODS

SSAs Generation for Single Particle Offline Analysis. Nascent SSA were generated from a wave-simulation channel facility containing filtered, Pacific Ocean seawater from the southern coast of California during the SeaSCAPE 2019 study.[5] The selected analysis was conducted on SSAs collected during a phytoplankton bloom that occurred from July 25th to August 14th.[5] To monitor phytoplankton growth throughout the experiment, continuous fluorescence measurements of chlorophyll-*a* (Chl-*a*) concentration were made *in situ* using a Sea Bird Scientific ECO-Triplet-BBFL2 sensor.[2,5] Daily bulk seawater samples were collected and stored for measurement of HB counts using a BD FACSCanto IITM flow cytometer.[2,5] Additional details of the wave flume experiment and SSA generation during the SeaSCAPE study can be found elsewhere.[5] A micro-orifice uniform deposit impactor (MOUDI; MSP, Inc., model 110) at a flow rate of 30 L/min was used to deposit individual submicrometer SSA onto hydrophobically coated (Rain-X) silicon substrates (Ted Pella, Inc.) at ca 80% relative humidity (RH).[2,10,55] MOUDI stages 7, 8, and 9 were used, corresponding to 50% cut-off aerodynamic diameter ranges of 0.32−0.56, 0.18−0.32, and 0.10−0.18 μm, respectively.[2] The substrate-deposited SSA samples were stored in clean Petri dishes and kept inside a laminar flow hood (NuAire, Inc., NU-425-400) at an ambient temperature (20−25 °C) and pressure prior to AFM and AFM−PTIR experiments.[2] The SSA samples collected during July 26th (pre-bloom), August 2nd (peak-bloom), and August 6th (post-bloom) were selected to investigate the size-dependent variability in SSA morphology, composition, phase state, and water uptake properties.

AFM Based Single Particle Morphology and OVF Measurements. A molecular force probe 3D AFM (Asylum Research, Santa Barbara, CA) was used for imaging a substrate-deposited individual SSA at ∼20% RH and ambient temperatures (20−25 °C).[2] Sample locations for single particle imaging were selected in a completely random and unbiased manner. A custom-made humidity cell was used to control RH with a range of 3%−80%.[2] For each RH value, a waiting time of at least 10 min was allocated prior to AFM measurements to ensure substrate-deposited SSA were in thermodynamic equilibrium with surrounding water vapor.[2] Silicon nitride AFM tips (MikroMasch, model CSC37, typical tip radius of curvature ∼10 nm, nominal spring constant 0.5−0.9 N/m) were used for imaging and force spectroscopy measurements.[2] AFM AC (tapping) mode imaging was used to collect height and phase images of individual SSA to determine their morphology, volume-equivalent diameter, and quantify the organic volume fraction (OVF) and organic coating thickness (OCT) for the core−shell SSA.[2,42] In this regard, approximately, 100−120 individual SSA were investigated for each sampling day.

The Igor Pro single particle analysis was used to measure the total particle volume from an AFM height image, which was then used to quantify its corresponding volume-equivalent diameter.[9,55] AFM phase images can reveal a spatially resolved degree of phase shift in AFM tip oscillations, which can be related to the difference in a viscoelastic nature within an individual SSA.[2,42] For an individual core−shell SSA, the phase image was used to determine the shell region and corresponding AFM height image was utilized to quantify the shell volume. The OVF for the core−shell SSA is defined as the ratio of shell volume to the total particle volume.[2,55] Assuming the core is predominantly inorganic, and the shell is organic, a single particle OVF value is reflective of the amount of organic relative to the amount of inorganic present in core−shell SSA. The volume-equivalent diameters determined for the total core−shell particle and the inorganic core region were then used to estimate the OCT, which represents the projected thickness of the organic shell around inorganic core.[2,56] The relative abundance (i.e., an average with one standard deviation for fraction of particles) of identified SSA main morphological categories (rounded, core−shell, prism-like, rod, and aggregate) and the average with one standard deviation of OVF and OCT values (obtained for 20−40 individual core−shell SSA) were recorded across the bloom for particles at three selected volume-equivalent diameter ranges (at ~20% RH) of 0.10−0.18, 0.18−0.32, and 0.32−0.60 μm.

AFM-Based Single Particle Water Uptake and Phase State Measurements. The water uptake was measured by recording a single particle hygroscopic growth factor (GF) at ~80% RH. The GF is defined as the ratio of the volume-equivalent diameter of an individual SSA, measured at ~80% RH, over the corresponding volume-equivalent diameter recorded at ~20% RH.[2] The GF measurements were performed on 5−8 individual SSAs from the most abundant morphologies at their highest corresponding relative occurrence size range (core−shell at 0.32−0.60 μm and rounded at 0.10−0.18 μm) across the bloom, and the values were reported as a range and average with one standard deviation.

Phase state identification at ~20 and 60% RH was performed using AFM force spectroscopy under ambient temperatures (20−25 °C) and pressure for core−shell, rounded, prism-like, and rod morphologies.[2,38,42] The RH values were selected as a benchmark based on previous phase state studies on sucrose that showed that solid to semisolid and semisolid to liquid phase transitions occur at ~20 and 60% RH, respectively.[38,42] AFM force spectroscopy measures the forces acting on the AFM tip versus tip-sample separation (i.e., force profiles); herein, a maximum applied force of 20 nN and scan rate of 0.8−1 Hz were utilized.[2] At least five force plots were collected by probing at the shell region of each core−shell SSA, and at an approximate center of each prism-like, rounded, and rod SSA at 20 and 60% RH. The collected force profiles were then used to quantify at a particular RH, the viscoelastic response distance (VRD, nm), which can be related to the viscoelastic nature of a solid (higher values generally correspond to lower viscosity), and the relative indentation depth (RID, ratio of the indentation depth over the particle height) for an individual particle.[2,42] A previously reported framework based on the VRD and RID measurements was then utilized to identify the phase state of each particle at a particular RH.[38] The VRD values measured on SSAs in the semisolid phase state were recorded as an average with one standard deviation for a particular morphology, volume-equivalent diameter, and RH throughout the bloom. Approximately, 20 individual SSAs for each morphology type were investigated for the phase identification.

Statistical Probability Distribution Analysis. As the total number of individual particles that can be practically studied with AFM is limited, we employed a statistical analysis to assess statistical significance of the measurements. Probability distributions associated with the likelihood of sampling one of the five particle morphology types, or one of the three phase states, were generated using a self-coded Monte Carlo-like simulation method.[57−60] Specifically, we first generated a "true" population of 10,000 particles in which the number of particles of a given type was specified as equal to the measured value for a given bloom state or size range. Then, we randomly sampled without replacement 10,000 sub-populations of *N* particles from this true distribution, where *N* is the actual number of sampled particles for a given bloom state or size range. Finally, probability distributions for each particle type were constructed from these 10,000 sub-populations. Hence, each graph represents the likelihood of obtaining a particular result across subpopulations. Next, an average with one standard deviation for a fraction of particles from each morphological type, or one of three phase states, was recorded across the bloom, RH, and volume-equivalent diameter range, by fitting the probability distribution plots with the Gaussian function. Data processing and analysis were conducted using Igor Pro (version 6.37, Wave metrics).

Single Particle Composition Using AFM−PTIR Measurements. AFM−PTIR measurements were conducted using a commercial nanoIR2 (Bruker, Santa Barbara, CA) microscope equipped with a tunable mid-IR quantum cascade laser (QCL) and a tunable mid-IR optical parametric oscillator laser (OPO). Experiments were performed at ~20% RH and ambient temperatures (23−26 °C) on SSA samples collected on MOUDI stages 7, 8, and 9 during July 26th (pre-bloom) and August 2nd (peak-bloom). AFM height images were collected in tapping mode at a scan rate of 0.5 Hz using silicon nitride probes with a chromium-gold coating (HQ: NSC19/CR-AU, MikroMasch, typical tip radius of curvature 35 nm, and a nominal spring constant range of 0.05−2.3 N/m). AFM−PTIR spectra were collected at a preselected tip-localized position across the sample surface with a nominal spatial resolution below 35 nm and a spectral resolution of 8 cm^{-1} (OPO) and 5 cm^{-1} (QCL), while co-averaging over 128 laser pulses. To account for a possible substrate contribution to the AFM−PTIR signal, a reference spectrum was taken on the substrate and subtracted from all corresponding spectra obtained on individual particles. Approximately, 10 individual SSAs with core−shell and rounded morphologies were investigated. For core−shell SSAs, spectra were taken at the core and shell particle regions, while for rounded SSAs, the spectra were taken at an approximate center of each particle.

Due to the large chemical diversity within a SSA, combining single particle spectra even with a similar morphology and size still results in a large variance. Thus, spectral results should not be viewed as confidently quantitative, but rather qualitatively demonstrate the presence (or potential absence) of a particular functional group within SSA.

Bulk Measurements of SSA Size-Dependent Organic and Inorganic Mass Fractions. For these measurements, SSAs were collected at 74−96% RH using a five stage SIOUTAS Personal Cascade Impactor (PCIS, SKC model 225−370 with 50% cut-off aerodynamic diameter ranges for each impactor stage of <0.25, 0.25−0.50, 0.50−1.0, 1.0−2.5, and >2.5 μm). A flow rate of 9 L/min was used with substrates consisting of pre-baked 25 mm Al foil disks for the top four stages (overall range of 0.25−≫2.5 μm) and a pre-baked 37 mm quartz fiber filter (QFF, PALL Life Sciences) for the lowest stage (<0.25 μm). Pre-bloom (July 26th) and peak-bloom (August 2nd) samples were collected for 46 and 23 h, respectively. All samples were stored frozen at −20 °C until the analysis. Organic carbon (OC) was measured using a thermal optical analyzer (Sunset Laboratories, Forest Grove, OR), as described previously.[10,61] The common inorganic ions were separated and quantified via high-performance ion exchange chromatography with conductivity detection (Dionex ICS5000, Sunnyvale, CA).[10,61,62] Substrates were sub-sampled using a stainless steel punch and extracted in 4 mL of ultrapure water (>18.2 MΩ·cm, Thermo Barnstead EasyPure II). QFFs were extracted with 30:40:30 min of shaking-sonication-shaking, respectively, while Al substrates were extracted by shaking for 100 min. All extracts were filtered (0.45 μm polypropylene, Whatman) prior to analysis. Anions and cations were identified against authentic standards (Dionex) and quantified with seven point calibration curves.[62] Inorganic mass was estimated as sea salt by converting the mass of sodium measured to the mass of sea salt using the sodium/sea salt ratio of 3.26, which was previously determined from seawater salt composition.[63]

■ RESULTS AND DISCUSSION

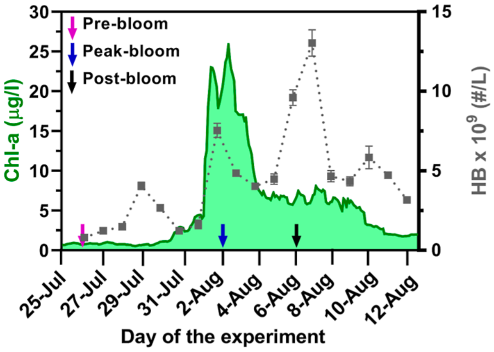

Figure 1. Temporal evolution of daily average concentrations over the course of mesocosm experiment for chlorophyll-*a* (Chl-*a*) (green) and HB with one standard deviation (gray squares and error bars). Purple, blue, and black arrows designate the three selected days for particle measurements during this study: Jul 26th (pre-bloom), Aug 2nd (peak-bloom) and Aug 6th (post-bloom), respectively.

Temporal Dependence of the Chlorophyll-*a* and HB Across the Phytoplankton Bloom. Figure 1 shows temporal dependence of daily average concentrations for chlorophyll-*a* (Chl-*a*) and HB of bloom 3, during the SeaSCAPE study.[5] The phytoplankton bloom progression in the wave flume was tracked by measuring the daily averaged Chl-*a* concentration. The Chl-*a* concentration was relatively low at the beginning of the study (average of 1 μg/L from July 25th to July 31st), then reached a maximum of 25 μg/L during the bloom peak on Aug 2nd, followed by a decrease thereafter (average of 5 μg/L from Aug 5th to Aug 13th).[5] The HB count was relatively low at the beginning of the study (average of 1.1 × 10^9 cells/L from July 25th to July 31st), and then increased during the bloom (7.6 × 10^9 cells/L on Aug 2nd), and reached its highest count after the bloom (12.9 × 10^9 cells/L on Aug 7th).[5] The Chl-*a* and HB concentration values, and their temporal behavior across the bloom studied here, were comparable with those observed during previous mesocosm experiments.[2,23,64,65] The SSA samples collected on July 26th (pre-bloom), Aug 2nd (peak-bloom), and Aug 6th (post-bloom) were selected to investigate the size-dependent relative distribution of bulk ensemble-averaged and single particle organic enrichment, single particle morphologies, compositions, phase states, and water uptake properties of SSA.

Bulk Ensemble-Averaged Size-Dependent Measurements of Organic Enrichment in SSA. The filter-based bulk ensemble-averaged method was used to investigate the size-dependent organic enrichment in SSA across the phytoplankton bloom. Figure 2A,B shows the bulk organic and inorganic mass fractions in SSA for pre-bloom and peak-bloom, respectively. Both days show an increase in the organic mass fraction with decreasing particle size. Specifically, during pre-bloom, the organic mass fraction increases with decreasing size, from 0.02 for SSA with sizes >0.25 μm to 0.39 for SSA with the sizes <0.25 μm. During peak-bloom, the organic mass fraction increases from below detection limit (BDL) for sizes >0.25 μm to 0.58 for sizes <0.25 μm. While these size-dependent trends are similar to previous observations from the field and mesocosm experiments,[10,66] absolute organic mass fraction values vary between each experiment.[19,29,67] Compared to pre-bloom SSA, peak-bloom SSA with a size range of 0.10−0.25 μm shows a modest increase in organic mass (ca 20%), which can be attributed to changes in seawater biological activity.[67,68] We note that the bulk measurements provide an ensemble-averaged value of the entire SSA population; however, they do not capture potential particle-to-particle variability in the organic enrichment. To both better understand the origin of observed organic enrichment in smaller SSA and to further correlate it with their physicochemical properties as well as to assess the particle-to-particle variability, single particle measurements were employed next.

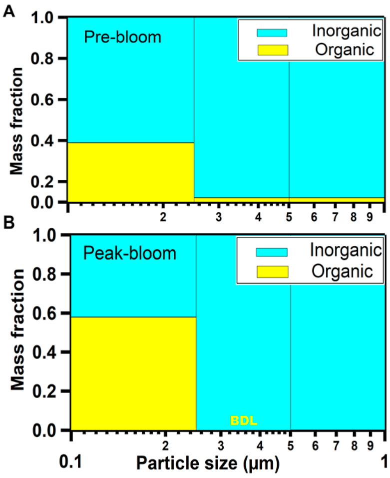

Figure 2. Organic (yellow) and inorganic (cyan) mass fractions versus particle size for (A) pre-bloom and (B) peak-bloom sampling days. The width of each bar indicates the SIOUTAS Personal Cascade Impactor cutoff size range at 74−96% RH. BDL indicates the measured organic mass fraction was below the detection limit.

Size-Dependent Morphological Distribution of SSA across the Bloom. Figure 3A shows the representative AFM height images of five main SSA morphological categories observed here: prism-like, core−shell, rounded, rod, and aggregate. For each sampling day, the characterized individual SSA were within the volume-equivalent diameter range of 0.10−0.60 μm. The morphological categorization was performed qualitatively using AFM height and phase images as described previously.[2,38,50,71,72] The identified main SSA morphological types were consistent with previous observations from the field and mesocosm experiments,[2,10,26,50] with some differences likely due to variability of the mixing states of individual particles.[10] The generating mechanism (i.e., film drops vs jet drops), and biological activity in the seawater can control the mixing states of SSA, which in turn determine SSA morphology, as demonstrated in prior studies.[26,34] Figure 3B shows the relative distribution of morphological categories across the bloom. The statistical probability distribution analysis was utilized to assess the relative distribution of each morphology type throughout the bloom (Figure S1), and as a function of size. From this analysis, we ascertained statistically significant differences in the relative abundancies for two main morphologies—rounded and core−shell SSA. Specifically, rounded SSAs were the most abundant during pre-bloom and peak-bloom, while core−shell SSAs were most abundant during pre-bloom and post-bloom. Across the bloom, the fraction of rounded SSA was similar during pre-bloom and

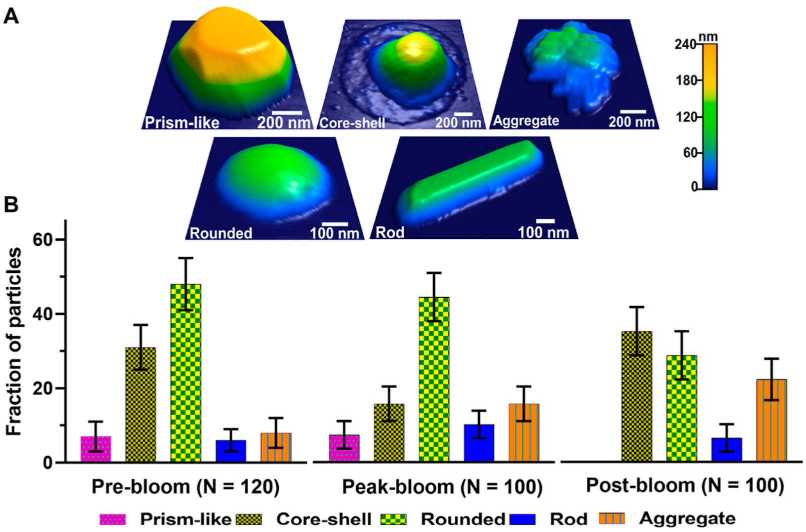

Figure 3. (A) Selected illustrative AFM 3D-height images of five main morphological categories (prism-like, core−shell, rounded, rod, and aggregate) identified for nascent SSA. The maximum height range is 240 nm for each image. (B) Average and one standard deviation of fraction of particles (%) from five main morphological categories during pre-bloom (120 particles), peak-bloom (100 particles) and post-bloom (100 particles) sampling days. For each bloom designated day, the characterized individual SSA had similar volume-equivalent diameter range of 0.10−0.60 μm.

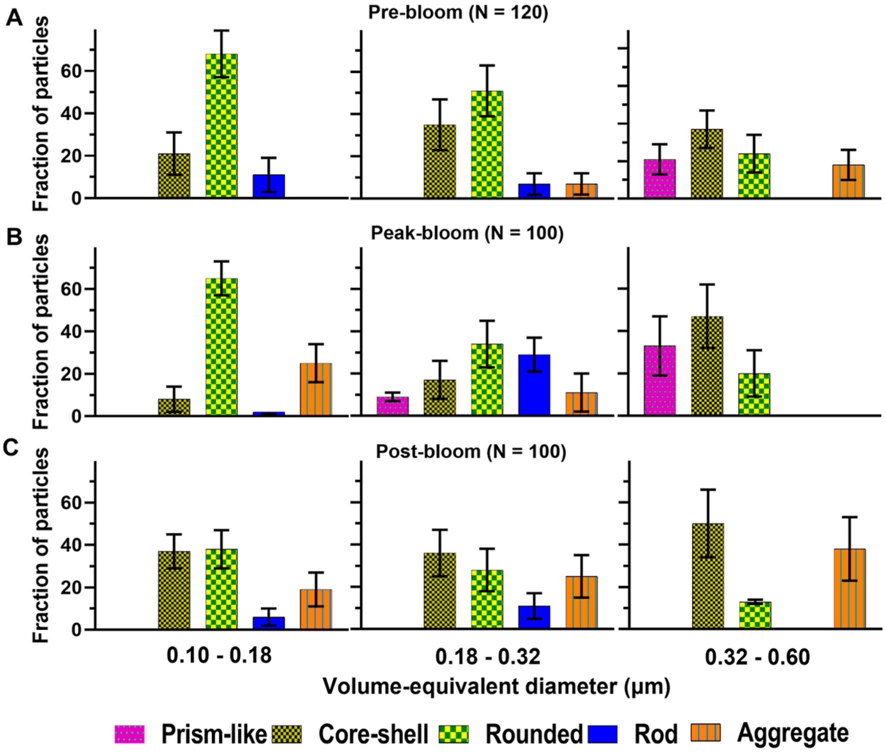

Figure 4. Average and one standard deviation of fraction of particles (%) from five main morphological categories of nascent SSA for three selected volume-equivalent diameter ranges of 0.10−0.18 (left), 0.18−0.32 (middle), and 0.32−0.60 μm (right) during (A) pre-bloom, (B) peak-bloom and (C) post-bloom sampling days.

peak-bloom and decreased during post-bloom. The fraction of core−shell SSA was approximately similar during pre-bloom and post-bloom, and decreased during peak-bloom. While the exact origin of observed SSA morphological variability during different stages of the bloom is still unclear, it likely originates from the change in seawater and SML chemical composition due to changes in seawater biological activity.

Figure 4 shows the size-dependent relative distribution of SSA morphologies within three selected volume-equivalent diameter ranges (0.10−0.18, 0.18−0.32, and 0.32−0.60 μm) during pre-bloom (Figure 4A), peak-bloom (Figure 4B), and post-bloom (Figure 4C). The statistical probability distribution plots to assess the distribution of morphology types across the size ranges and sampling days are shown in Figure S2. During pre-bloom and peak-bloom, the majority of smaller SSA was rounded, while larger SSA was predominantly core−shell. For post-bloom, smaller SSAs showed similar abundance of rounded and core−shell morphologies, while larger SSAs were predominantly core−shell. Prism-like morphology was the most abundant in larger SSAs. The abundance of rod and aggregate morphologies fluctuated across the size ranges and sampling days. Moreover, the SSA studied here with sizes between 0.10 and 0.32 μm likely corresponds to film drops (typical dry diameter $\leq$ 0.25 μm) and enriched with organic species, while SSAs with sizes of 0.32 and 0.60 μm likely originate from jet drops (typical dry diameter $\geq$ 0.25 μm) and are thus predominantly inorganic.[21]

To provide context for the observed variability of SSA morphological types and their size-dependent relative abundance across the bloom, we can compare our results with previous wave flume experiments.[2,10,50] Prior studies performed on submicrometer nascent SSA during the phytoplankton blooms identified sea salt-organic (equivalent to core−shell) as the predominant SSA morphology, followed by homogenous organic (equivalent to rounded), organic-salt agglomerate (equivalent to aggregate), and needle-like particles (equivalent to rod).[2,26,50] Another study conducted on a submicrometer nascent SSA in the absence of a phytoplankton bloom displayed an increasing abundance of rounded and concurrent decrease of prism-like SSA as particle size decreases, consistent with the current study.[10] While observed SSA morphologies during the current study were consistent with previous studies, the differences in their relative abundances between various mesocosm experiments are likely due to variations in seawater composition, biological activity, and aerosol generation methods.[2,10,26,50,69]

AFM-based single particle size-dependent OVF and corresponding OCT of core−shell SSA at 20% RH across the bloom are summarized in Figure 5 and Table 1, respectively. As will be demonstrated in the next section using AFM−PTIR, the core and shell regions of core−shell SSA are predominantly inorganic and organic, respectively.[70] Thus, larger OVF values are indicative of a relatively higher organic content in the core−shell SSA. For each sampling day, the average OVF increases with decreasing particle size, implying organic enrichment in a smaller core−shell SSA. Additionally, a modest increase of the average OVF across the bloom was observed, and the values are consistent with prior wave flume experiments.[2] Based on the average OVF results, corresponding OCT were calculated. Across the bloom, core−shell SSA displayed modest OCT variability (15−20 nm range). Comparatively, with respect to the particle size, the larger core−shell SSA displayed relatively thinner OCT compared to relatively thicker OCT for smaller SSA, which is consistent with previous studies.[10]

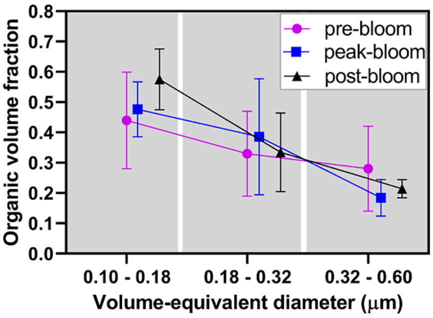

Figure 5. Averaged organic volume fraction measured using AFM at 20% RH for core−shell individual SSA at three selected volume-equivalent diameter ranges of 0.10−0.18, 0.18−0.32, and 0.32−0.60 μm during pre-bloom (purple circles), peak-bloom (blue squares) and post-bloom (black triangles) sampling days. Symbols and error bars represent the average and one standard deviation, respectively (listed in Table 1). The solid lines are shown for illustrative purposes only.

Single Particle SSA Morphology and Composition. Figure 6 shows the AFM−PTIR spectra taken on core−shell and rounded SSA particles for three selected volume-equivalent diameter ranges of 0.10−0.18, 0.18−0.32, and 0.32−0.60 μm during pre-bloom and peak-bloom. Due to the small volume of material contained in each particle and relatively low IR signal associated with the organic compounds, the resulting AFM−PTIR spectra show peaks that are broad and low in intensity. The most common organic functional groups associated with spectral features observed include peaks in the 1000−1200 cm^{-1} region, which is related to the stretching motion associated with ν(C−O−C) or ν(C−O); peaks in the 1350−1450 cm^{-1} region associated with δ(CH_2,CH_3), or ν_s(COO^-); and peaks in the 1550−1750 cm^{-1} region associated with ν(C=C), ν(C=O), or ν_{as}(COO^-).[73−76]

Past mesocosm studies involving marine SSA have demonstrated the presence and enrichment of organic compounds such as complex sugars and longer hydrocarbon chain *n*-alkanes in submicron SSA.[3,25,77] Reference spectra for a few representative compounds within these broader classes are provided in Figure S3A, including sodium nitrate and sulfate salts, aliphatic compounds (docosane), simple sugars (sucrose), and complex sugars (lipopolysaccharide and sodium alginate). We note that the PTIR spectral results are not unambiguously suggesting the presence of these specific reference compounds, but a more likely mixture of numerous species contained within these broader encompassing classes, the exact identification of which is impossible with the PTIR spectra.

Figure 6A shows the PTIR spectra for pre-bloom core−shell SSAs. The particle spectra in the shell region display no major spectral differences as a function of size within the studied size range of 0.10−0.60 μm. In some cases, the spectral signatures are similar to complex sugars (Figure S3A), but the more intense δ(CH_2,CH_3) modes suggest the presence of more aliphatic species. The enrichment of these complex sugars is consistent with prior studies performed on submicrometer nascent SSAs.[3,25,32,77] The core of the 0.18−0.32 and 0.32−0.60 μm size particles are spectrally similar to the corresponding shells, suggesting that organic coatings extend onto the core surface of the particle. However, in the smaller sized SSA, 0.10−0.18 μm, the core is seen to be nearly IR inactive, likely implying absence of the organic coating on the core or a very thin organic coating.

Spectra of peak-bloom core−shell SSA are shown in Figure 6B. Shells of the 0.10−0.18 and 0.18−0.32 μm size particles are similar to those observed in pre-bloom. This suggests that these particle shells are largely organic, including complex sugars and aliphatic compounds. Similar features are observed in the 0.10−0.18 μm size SSA cores, suggesting the presence of organic coatings, while the 0.18−0.32 μm SSA cores contain a single peak around 1020 cm^{-1}, potentially associated with the presence of a thin coating of simple sugars (e.g., sucrose Figure S3A) or silicates,[78,79] but accurate assignment is difficult due to low absorbances in the higher wavenumber modes. The larger

Table 1. Summary of Bloom Designation for Three Selected Volume-Equivalent Diameter Ranges for Core−Shell SSA at 20 and 60% RH, Averaged and One Standard Deviation for Fraction of Particles at Solid, Semisolid, and Liquid Phase States, VRD for the Shell, OVF, OCT, Volume-Equivalent GF, and Hygroscopicity Parameter ($\kappa_{mixture}$)

core−shell		fraction of particles at specified phase state (%)								
bloom designation (diameter range, μm)	RH (%)	solid	semisolid	liquid	VRD[a] (nm)	OVF	OCT (nm)	GF (80% RH)	GF range (80% RH)	$\kappa_{mixture}$ (80% RH)
					pre-bloom					
0.10−0.18	20	14 ± 22	86 ± 16	0	3.6 ± 4.2	0.44 ± 0.16	15 ± 6			
	60	0	57 ± 23	43 ± 24	4.3 ± 4.2					
0.18−0.32	20	29 ± 22	71 ± 21	0	1.4 ± 1.3	0.33 ± 0.14	16 ± 9			
	60	0	57 ± 23	43 ± 24	3.0 ± 4.5					
0.32−0.60	20	50 ± 24	50 ± 24	0	0.5 ± 0.1	0.28 ± 0.14	20 ± 10	1.5 ± 0.1	1.3−1.7	0.6 ± 0.3
	60	0	100	0	3.2 ± 1.6					
					peak-bloom					
0.10−0.18	20	0	100	0	0.9 ± 0.3	0.47 ± 0.09	15 ± 5			
	60	0	100	0	15.2 ± 7.5					
0.18−0.32	20	50 ± 23	50 ± 23	0	0.9 ± 0.2	0.38 ± 0.19	17 ± 9			
	60	0	100	0	1.2 ± 0.2					
0.32−0.60	20	43 ± 24	57 ± 23	0	0.7 ± 0.1	0.18 ± 0.06	16 ± 3	1.3 ± 0.1	1.2−1.4	0.3 ± 0.2
	60	0	100	0	8.2 ± 7.5					
					post-bloom					
0.10−0.18	20	53 ± 23	47 ± 23	0	0.7 ± 0.3	0.58 ± 0.10	19 ± 7			
	60	0	62 ± 23	38 ± 23	2.5 ± 2.0					
0.18−0.32	20	70 ± 21	30 ± 21	0	1.0 ± 0.7	0.34 ± 0.13	17 ± 7			
	60	0	75 ± 19	25 ± 21	3.3 ± 5.8					
0.32−0.60	20	71 ± 19	29 ± 20	0	0.6 ± 0.2	0.22 ± 0.03	15 ± 3	1.6 ± 0.1	1.5−1.8	0.8 ± 0.2
	60	0	20 ± 21	80 ± 18	1.7 ± 2.4					

[a] Data range reported only for core−shell particles with organic coating at semisolid phase state.

0.32−0.60 μm size particles from peak-bloom are more spectrally distinct. From the shell, there are absorbances around 1300−1450 cm^{-1} with no detectible peaks at 1550−1700 cm^{-1}, suggesting that these coatings have a low degree of unsaturation (C═C) or oxygen (C═O) content, and more largely comprised of contributions from $\delta(CH_2,CH_3)$ due to a larger fraction of aliphatic species, such as *n*-alkanes (Figure S3B).[3,80] The same spectral features are also present on the particle core, suggesting similar organic coatings as in the shell, in addition to an intense sharp peak at 1380 cm^{-1}, potentially due to nitrates.[81,82]

PTIR spectra for rounded SSA are shown in Figure 6C,D, where similar vibrational modes and peak shapes associated with complex sugars (Figure S3A) are observed across all size ranges. Most notably, there are two broad peaks centered around 1615−1650 and 1435 cm^{-1}. Slight differences are seen in the peak ratios between pre-bloom and peak-bloom spectra, where peak-bloom rounded SSAs exhibit a larger mode around 1550−1700 cm^{-1} relative to the $\delta(CH_2,CH_3)$ mode around 1435 cm^{-1}, suggesting a higher degree of C═C or C═O content relative to pre-bloom rounded SSA.[73,76] The PTIR spectra collected for prism-like and rod particles are shown in Figure S4. The rods were only analyzed within the smallest size range (0.10−0.18 μm) and the spectra are characterized by a sharp mode around 1170 cm^{-1} associated with $\nu_{as}(SO_4^{2-})$ from inorganic sulfates (Figure S3B).[83] The larger size (0.32−0.60 μm) prism-like particles are IR inactive as detected by AFM−PTIR. However, in smaller prism-like particles (0.18−0.32 μm), there is spectral evidence for nitrates, around 1355 and 1380 cm^{-1}, that overlap well with measured nitrate spectra (Figure S3B), and the asymmetric nitrate stretching motion $\nu(NO_3^-)$.[83,84] These spectral features agree well with their corresponding sodium salts, as shown in Figure S4A. The particles with prism-like morphologies thus are expected to be relatively low in organic content as detected by AFM−PTIR.

Particle-to-particle variability in chemical composition is demonstrated in Figure S5A, where PTIR spectra were taken on three different rounded particles, each with the same volume-equivalent diameter of 0.18 μm. Rounded particles shown in Figure S5B are spectrally distinct from each other. Chemical maps reveal that the absorbance of 1640 and 1450 cm^{-1} modes corelates with particle height, and the particles spectrally appear to be of uniform composition. Figure S5C is a rounded particle with no distinct morphological indication of phase separation. However, the spectra and chemical maps reveal two different regions within the particle, where one region is enriched with organics that are complex sugars, while another region spectrally shows that aliphatic compounds are more abundantly present.

Figure 7 summarizes the key AFM−PTIR spectroscopic results that core−shell and rounded SSA are primarily enriched with organic components, such as complex sugars and aliphatic compounds, while prism-like and rod morphologies are predominantly inorganic salts with relatively low organic content. Single particle morphology and composition measurements can be compared with the bulk-ensemble average organic mass fraction measurements described above. Collectively, the increase of bulk organic mass fraction as particle size decreases (Figure 2) can be attributed to a combination of an increase in relative abundance of predominantly organic rounded SSA and higher OVF values for core−shell SSA with size reduction.

Morphology and Size-Dependent Phase State, and Water Uptake of SSA across the Bloom. AFM force

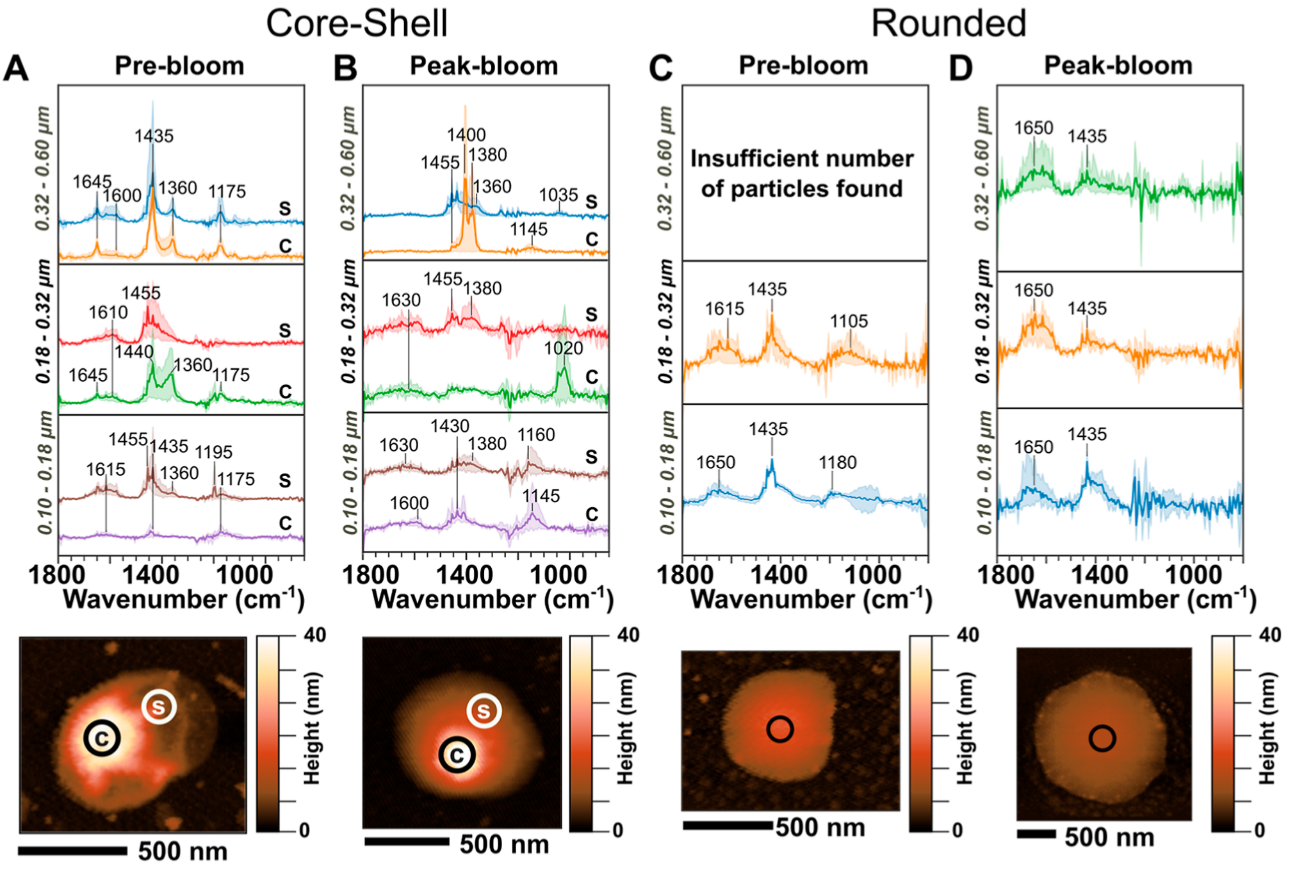

Figure 6. PTIR spectra and representative AFM height images for core−shell and rounded SSA measured using AFM-IR for (A,C) pre-bloom and (B,D) peak-bloom days. SSA spectra are divided into three selected volume-equivalent diameter ranges of 0.10−0.18, 0.18−0.32, and 0.32−0.60 μm. For core−shell SSA, spectra were taken at two positions: in the core (C) and shell (S). For rounded SSA, spectra were taken at an approximate center of each particle. Solid lines show the average spectra (at least 3 particles) for a particular morphology/particle region and shaded lines representing one standard deviation.

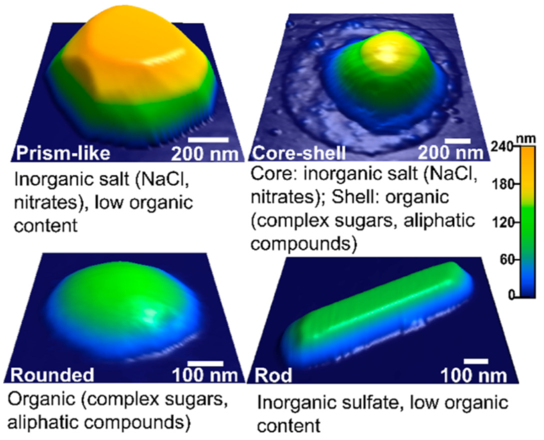

Figure 7. Representative AFM 3D-height images at 20% RH of nascent SSA (volume-equivalent diameter range 0.10−0.60 μm) four main morphological categories across the bloom with corresponding chemical composition determined by AFM−PTIR. The maximum height range is 240 nm for each AFM image.

spectroscopy (i.e., force profiles) was utilized to investigate the phase state of individual rounded, core−shell, prism-like, and rod SSA at three selected volume-equivalent diameter ranges (0.10−0.18, 0.18−0.32, and 0.32−0.60 μm) collected across the bloom. Briefly, single particle force profiles at 20 and 60% RH were obtained by probing at the shell region of each core−shell, and at an approximate particle center for other morphologies. The force profiles were then used to quantify the VRD (nm) and RID for each particle at corresponding RH.[2,38,42] A previously reported framework based on the VRD and RID measurements was then utilized to identify the phase state of each particle at a particular RH.[38]

Figure 8 and Table 1 show the size-dependent relative distribution of solid, semisolid, and liquid phase states for the shell region of core−shell SSA along with the VRD values measured on semisolid shells. Figure S6 shows the statistical probability distribution plots of solid, semisolid, and liquid phase states for the shells across the bloom at three size ranges. At 20% RH, the abundance of larger core−shell SSA with solid shells increased across the bloom. Moreover, during each sampling day, at 20% RH, the abundance of semisolid shells increased as particle size decreased. Additionally, with decreasing size, semisolid shells from pre-bloom likely became less viscous as evidenced by increasing VRD values (Table 1), while those from peak-bloom and post-bloom displayed no clear size-dependent variability. As RH increased to 60%, shells uptake water, becoming more hydrated and less viscous as shown by increased corresponding VRD values relative to 20% RH.[2,9,38] At 60% RH, shells from peak-bloom were semisolid across all sizes, while those from pre-bloom and post-bloom were either more semisolid or liquid as particle size decreases. A previous study performed to investigate the phase state of core−shell nascent SSA (volume-equivalent diameter range of

https://doi.org/10.1021/acsearthspacechem.1c00306
ACS Earth Space Chem. 2022, 6, 116−130

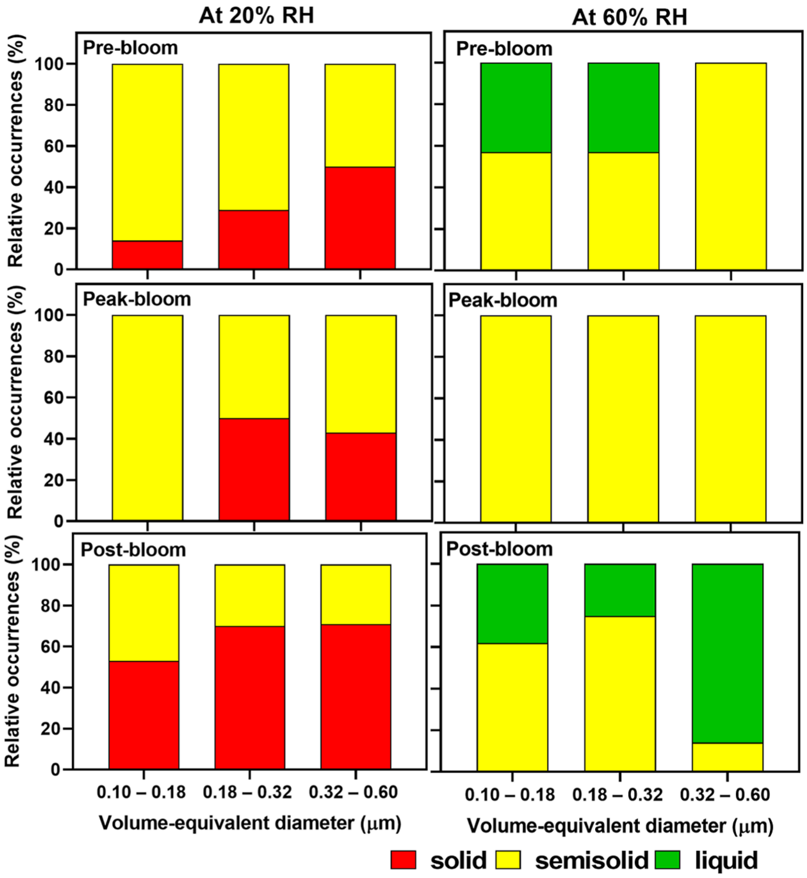

Figure 8. Relative distributions of solid, semisolid, and liquid phase states at 20% (left) and 60% (right) RH for the shell region of core−shell SSA at three selected volume-equivalent diameter ranges of 0.10−0.18, 0.18−0.32, and 0.32−0.60 μm across the bloom.

0.3−1 μm) showed that the majority of shells during a bloom were semisolid at 20 and 60% RH, which is consistent with the observation for peak-bloom from the current study.[2]

Figure 9 and Table 2 show the size-dependent relative distribution of phase states for rounded SSA, along with the VRD values measured on semisolid particles. Figure S7 shows the statistical probability distribution plots of solid, semisolid, and liquid phase states for rounded SSAs across the bloom at three size ranges. At 20% RH, the abundance of larger rounded SSA with a semisolid phase state increased across the bloom. At 20% RH, with decreasing size, the abundance of solid rounded SSA increased for peak-bloom and post-bloom. Furthermore, the VRD values (at 20% RH) collected on semisolid rounded SSA during each sampling day did not display any clear size dependence. As RH increased to 60%, rounded SSA uptake water and become less viscous as evidenced by increased corresponding VRD values relative to 20% RH. At 60% RH, pre-bloom had the highest abundance of rounded SSA at liquid phase state, compared to peak-bloom and post-bloom where majority of rounded SSA showed semisolid phase state. The observed size-dependent phase state changes in shells of core−shell and rounded SSA throughout the bloom can be attributed to the variability of organic and inorganic compounds present within each particle at varying concentrations and different mixing states, as demonstrated by the AFM−PTIR measurements above.

Because no apparent size-dependent phase state was observed for prism-like and rod SSAs, the results were combined over a wider volume-equivalent size range of 0.10−0.60 μm at 20 and 60% RH for each sampling day. At 20% RH, prism-like SSA from pre-bloom and peak-bloom predominantly showed solid phase state, and some particles became semisolid at 60% RH. Prior studies have shown that sodium chloride particles can exhibit prism-like morphology, with solid phase state at both 20 and 60% RH.[38,42] Therefore, the semisolid phase state of some prism-like SSA in this study likely originates from the presence of thin organic coatings on the particles, as also evidenced by the AFM−PTIR spectra above. At 20% RH, rod SSA showed predominantly solid phase state across the bloom, and a small fraction of rods became semisolid as RH increased to 60%. The chemical composition and phase state data confirmed that the rod SSA are not bacteria cells. Overall, these results collectively demonstrate that the phase state of SSA is dynamic and varies depending on the particle morphology (mixing state), chemical composition, size, RH, and the seawater biological activity. This should be considered in future studies to better understand and more accurately predict SSA's ability to act as efficient CCN or IN.

The measured GF and calculated hygroscopicity parameter (κ_{mixture}) of core−shell and rounded SSA were investigated at 80% RH using a previously validated AFM-based approach.[2,9,35,40,85] Table 1 summarizes the results for core−shell SSA at the highest relative occurrence size range (0.32−0.60 μm) across the bloom. The 80% RH was selected because it is above the deliquescence point of pure NaCl (~75% RH), thus assuming the core of core−shell SSA is primarily NaCl, such particles are expected to undergo a complete deliquescence to form liquid droplets.[9] An unpaired *t*-test (*P*

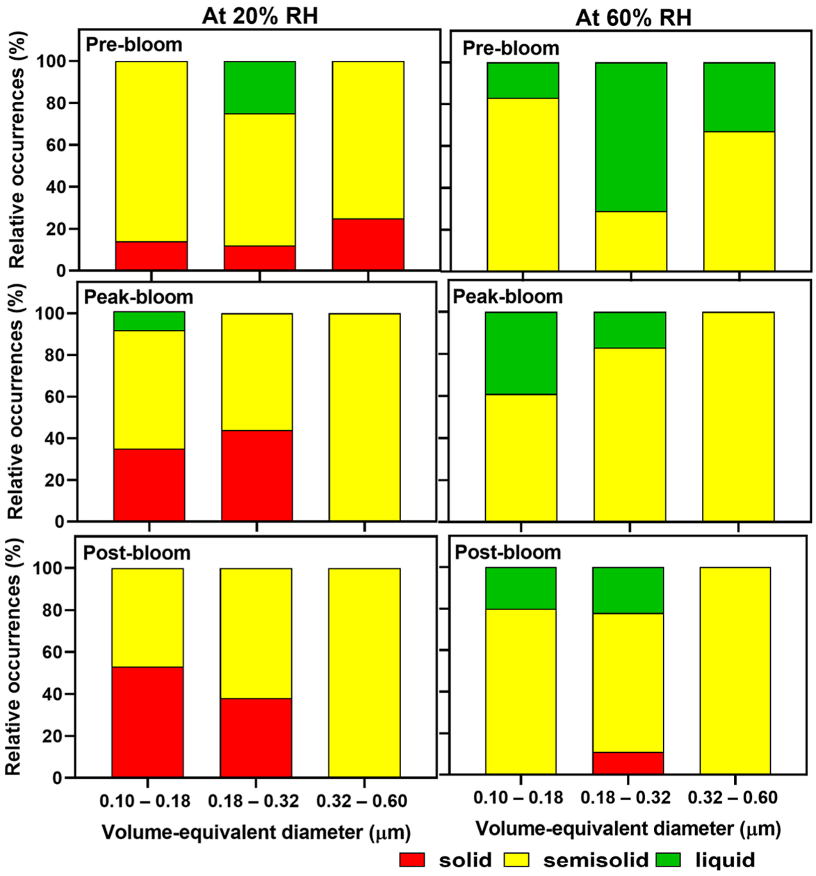

Figure 9. Relative distributions of solid, semisolid, and liquid phase states at 20% (left) and 60% (right) RH for rounded SSA at three selected volume-equivalent diameter ranges of 0.10−0.18, 0.18−0.32, and 0.32−0.60 μm across the bloom.

< 0.05) was conducted between each sampling day, and the results confirmed a statistically significant difference of the GF values between peak and post-bloom days. The observed GF and $\kappa_{\mathrm{mixture}}$ values were consistent with previous studies on model and nascent SSA.[2,9,35,86] In particular, the range of GF and $\kappa_{\mathrm{mixture}}$ values determined in this study overlaps well with SSA-relevant two-component systems of NaCl/sodium alginate, and NaCl/lipposaccharides at various mass fractions.[35] The variation of GF and $\kappa_{\mathrm{mixture}}$ in core−shell SSA during each sampling day is likely due to varying concentrations of various organic species with different hygroscopicities.[2] Table 2 summarizes the GF and $\kappa_{\mathrm{mixture}}$ values collected on rounded SSA at the highest relative occurrence size range (0.10−0.18 μm) during each sampling day. The average GF and $\kappa_{\mathrm{mixture}}$ values did not vary over sampling days and were consistent with previous studies on model SSA-relevant systems, such as sodium alginate, lipposaccharides, and laminarin.[3] The rounded SSAs studied here were smaller in range compared to that of the core−shell SSA. Notably, the GF values of rounded SSA were ~27% lower than that of the core−shell SSA that contain a hygroscopic inorganic core (average of 1.50). Additionally, the variability of GF range in rounded SSA during each sampling day is likely due to variability in particle-to-particle organic speciation and mixing states with different hygroscopicities.

■ SUMMARY AND CONCLUSIONS

The current study investigated size-dependent particle-to-particle variability of submicrometer nascent SSA morphology, composition, mixing state, phase state, and water uptake properties, as a function of RH and seawater biological activity. AFM imaging identified five main SSA morphologies present in 0.10−0.60 μm size range across the bloom: prism-like, core−shell, rounded, rod, and aggregate. Of these morphologies, approximately 70% of SSA throughout the bloom were core−shell and rounded particles. Moreover, the majority of smaller SSA were rounded, while larger SSA showed predominantly a core−shell morphology. Filter-based measurements revealed increased organic enrichment in smaller SSA, which AFM−PTIR attributed to the presence of complex sugars and alkanes in rounded and core−shell SSA. Prism-like and rod SSAs were identified as predominantly inorganic salts with relatively low organic content. These findings reveal a significant variability in SSA morphology, mixing states, and chemical composition with respect to particle size, and seawater biological activity. Because morphology, mixing states, and chemical composition can alter SSA's water uptake and phase states properties, it is important to determine these size-dependent relationships to better understand the impact of SSA on climate-relevant processes such as their CCN ability.[10,39]

To the best of our knowledge, the size-dependent phase state measurements of SSA presented herein were performed for the first time, and results showed a significant variability in the phase state with respect to SSA morphology, size, RH, and seawater biological activity. At 20% RH, the core−shell SSA across the bloom showed an increase in the relative abundance of semisolid shells as size decreased, while the rounded SSA were increasingly more solid (for peak and post-bloom) or

Table 2. Summary of Bloom Designation for Three Selected Volume-Equivalent Diameter Ranges for Rounded SSA at 20 and 60% RH, Averaged and One Standard Deviation for Fraction of Particles at Solid, Semisolid, and Liquid Phase States, VRD, Volume-Equivalent GF, and Hygroscopicity Parameter ($\kappa_{\mathrm{mixture}}$)

rounded		fraction of particles at specified phase state (%)						
bloom designation (diameter range, μm)	RH (%)	solid	semisolid	liquid	VRD[a] (nm)	GF (80% RH)	GF range (80% RH)	$\kappa_{\mathrm{mixture}}$ (80% RH)
			pre-bloom					
0.10−0.18	20	14 ± 21	86 ± 16	0	2.1 ± 1.7	1.1 ± 0.1	1.0−1.3	0.1 ± 0.1
	60	0	83 ± 22	17 ± 20	2.4 ± 1.4			
0.18−0.32	20	12 ± 22	63 ± 24	25 ± 20	1.5 ± 1.2			
	60	0	29 ± 21	71 ± 23	2.1 ± 1.0			
0.32−0.6	20	25 ± 21	75 ± 19	0	1.3 ± 0.7			
	60	0	67 ± 22	33 ± 22	1.9 ± 0.7			
			Peak-bloom					
0.10−0.18	20	35 ± 13	57 ± 14	9 ± 1	1.5 ± 1.3	1.1 ± 0.1	1.0−1.2	0.1 ± 0.1
	60	0	61 ± 13	39 ± 13	1.6 ± 1.1			
0.18−0.32	20	44 ± 24	56 ± 24	0	1.3 ± 1.2			
	60	0	83 ± 10	17 ± 10	2.1 ± 1.6			
0.32−0.6	20	0	100	0	1.5 ± 1.3			
	60	0	100	0	5.6 ± 0.1			
			Post-bloom					
0.10−0.18	20	53 ± 16	47 ± 16	0	0.8 ± 0.5	1.1 ± 0.1	1.0−1.4	0.1 ± 0.1
	60	0	80 ± 12	20 ± 12	2.7 ± 1.9			
0.18−0.32	20	38 ± 13	62 ± 13	0	2.2 ± 1.7			
	60	11 ± 9	67 ± 22	22 ± 21	4.4 ± 2.4			
0.32−0.6	20	0	100	0	0.8 ± 0.4			
	60	0	100	0	2.6 ± 0.6			

[a] Data range reported only for rounded particles at semisolid phase state.

semisolid (for pre-bloom), as particle size decreased. As RH increased to 60%, shells of core−shell and rounded SSA uptake water, becoming less viscous, and their corresponding phase state changes into either semisolid or liquid. Additionally, prism-like and rod SSAs were primarily solid at 20% RH, and some became semisolid at 60% RH likely due to the presence of a thin organic coating on the particle surface. The statistical analysis performed on the size-dependent variability of SSA morphologies and phase states across the bloom confirmed statistical significance of the measurements, despite the finite number of individual particles studied with AFM for each sample. Size-dependent phase state information can facilitate better understanding of SSA's climate-relevant effects such as light scattering efficiency, CCN ability, and atmospheric chemical aging. For example, during atmospheric chemical aging, the characteristic mass-transport time of different atmospheric gases strongly depends on a particular phase state and viscosity of SSA.[15,43,87,88] Because our results demonstrate significant variability of SSA phase state with respect to the morphology, size, and seawater biological activity, the timescale to undergo chemical aging will be different. Additionally, the size-dependent variability in phase state will modulate the diffusion length of water molecules within SSA at a particular atmospheric RH, which may alter or even suppress their water uptake, therefore change the strength of direct radiative forcing.

Noteworthily, our results illustrate a significant limitation of utilizing an approach that assumes a particular representative nascent submicrometer SSA morphology and phase state across a phytoplankton bloom over an entire size range. Instead, there is a complex and dynamic interplay between SSA size-dependent physicochemical properties which must be considered in future field studies and during the selection of model systems to investigate SSA's atmospheric impacts. Significantly, owing to the size-dependent nature of these properties, studies focusing on larger SSA cannot be readily extrapolated to smaller size ranges (e.g., supermicrometer vs submicrometer). Instead, detailed information on the extent of particle-to-particle variability and size-dependent nature of SSA morphology, composition, mixing state, phase state, and water uptake is expected to facilitate more accurate quantification and prediction of SSA's climate-related effects.

■ ASSOCIATED CONTENT

Supporting Information

The Supporting Information is available free of charge at https://pubs.acs.org/doi/10.1021/acsearthspacechem.1c00306.

> Details of AFM−PTIR spectra taken for spectrally distinct rounded particles, and prism and rod particles, AFM−PTIR spectra taken for laboratory deposited reference compounds, details of statistical probability distribution plots for various SSA morphology types, and phase states across the bloom and as a function of particle size (PDF)

■ AUTHOR INFORMATION

Corresponding Author

Alexei V. Tivanski − *Department of Chemistry, University of Iowa, Iowa City, Iowa 52242, United States;* orcid.org/0000-0002-1528-2421; Email: alexei-tivanski@uiowa.edu

Authors

Chathuri P. Kaluarachchi − *Department of Chemistry, University of Iowa, Iowa City, Iowa 52242, United States;* orcid.org/0000-0003-2538-3952

Victor W. Or − *Department of Chemistry and Biochemistry, University of California, San Diego, La Jolla, California 92093, United States*

Yiling Lan − *Department of Chemistry, University of Iowa, Iowa City, Iowa 52242, United States*

Chamika K. Madawala − *Department of Chemistry, University of Iowa, Iowa City, Iowa 52242, United States*

Elias S. Hasenecz − *Department of Chemistry, University of Iowa, Iowa City, Iowa 52242, United States*

Daniel R. Crocker − *Department of Chemistry and Biochemistry, University of California, San Diego, La Jolla, California 92093, United States;* orcid.org/0000-0002-5297-1103

Clare K. Morris − *Scripps Institution of Oceanography, University of California, San Diego, La Jolla, California 92093, United States*

Hansol D. Lee − *Department of Chemistry, University of Iowa, Iowa City, Iowa 52242, United States;* orcid.org/0000-0002-2091-776X

Kathryn J. Mayer − *Department of Chemistry and Biochemistry, University of California, San Diego, La Jolla, California 92093, United States*

Jonathan S. Sauer − *Department of Chemistry and Biochemistry, University of California, San Diego, La Jolla, California 92093, United States*

Christopher Lee − *Scripps Institution of Oceanography, University of California, San Diego, La Jolla, California 92093, United States*

Glorianne Dorce − *Department of Chemistry, University of Iowa, Iowa City, Iowa 52242, United States*

Francesca Malfatti − *Scripps Institution of Oceanography, University of California, San Diego, La Jolla, California 92093, United States; Department of Life Science, Universita' Degli Studi di Trieste, Trieste 34127, Italy*

Elizabeth A. Stone − *Department of Chemistry, University of Iowa, Iowa City, Iowa 52242, United States;* orcid.org/0000-0003-0078-141X

Christopher D. Cappa − *Department of Civil and Environmental Engineering, University of California, Davis, Davis, California 95616, United States;* orcid.org/0000-0002-3528-3368

Vicki H. Grassian − *Department of Chemistry and Biochemistry and Scripps Institution of Oceanography, University of California, San Diego, La Jolla, California 92093, United States;* orcid.org/0000-0001-5052-0045

Kimberly A. Prather − *Department of Chemistry and Biochemistry and Scripps Institution of Oceanography, University of California, San Diego, La Jolla, California 92093, United States*

Complete contact information is available at: https://pubs.acs.org/10.1021/acsearthspacechem.1c00306

Author Contributions

The manuscript was written through contributions of all authors. All authors have given approval to the final version of the manuscript. Project administration: K.A.P., V.H.G., C.D.C., F.M., E.A.S., and A.V.T. Sample and data collection: C.P.K., V.W.O., C.M., Y.L., E.S.H., D.R.C., G.D., and C.K.M. Writing: C.P.K., V.W.O., E.S.H., D.R.C., H.D.L., K.J.M., J.S.S., C.L., F.M., E.A.S, C.D.C., V.H.G., K.A.P., and A.V.T.

Notes

The authors declare no competing financial interest.

Any opinions, findings, and conclusions or recommendations expressed in this material are those of the authors and do not necessarily reflect the views of the National Science Foundation. The data for this publication can be retrieved from the UC San Diego Library Digital Collections. https://doi.org/10.6075/J04748D9.

■ ACKNOWLEDGMENTS

This work was funded by the Center for Aerosol Impacts on Chemistry of the Environment (CAICE), a National Science Foundation (NSF) Center for Chemical Innovation (CHE-1801971). The authors thank the entire SeaSCAPE team for their hard work, and especially Dr. Kathryn Mayer, Dr. Jon Sauer, Prof. Timothy Bertram, and Prof. Christopher Cappa for designing and overseeing the campaign. A full list of participants can be found online: https://caice.ucsd.edu/experiment-campaigns/. The authors thank Ruochen Cao and Jiawei Yin for contributing to analysis of the Chl-*a* dataset. C.P.K. was partially supported by a University of Iowa Graduate College Summer Fellowship and University of Iowa Graduate College Post-Comprehensive Fellowship.

■ REFERENCES

(1) Bertram, T. H.; Cochran, R. E.; Grassian, V. H.; Stone, E. A. Sea spray aerosol chemical composition: elemental and molecular mimics for laboratory studies of heterogeneous and multiphase reactions. *Chem. Soc. Rev.* **2018**, *47*, 2374−2400.

(2) Lee, H. D.; Morris, H. S.; Laskina, O.; Sultana, C. M.; Lee, C.; Jayarathne, T.; Cox, J. L.; Wang, X.; Hasenecz, E. S.; DeMott, P. J.; Bertram, T. H.; Cappa, C. D.; Stone, E. A.; Prather, K. A.; Grassian, V. H.; Tivanski, A. V. Organic Enrichment, Physical Phase State, and Surface Tension Depression of Nascent Core-Shell Sea Spray Aerosols during Two Phytoplankton Blooms. *Acs Earth Space Chem.* **2020**, *4*, 650−660.

(3) Cochran, R. E.; Laskina, O.; Trueblood, J. V.; Estillore, A. D.; Morris, H. S.; Jayarathne, T.; Sultana, C. M.; Lee, C.; Lin, P.; Laskin, J.; Laskin, A.; Dowling, J. A.; Qin, Z.; Cappa, C. D.; Bertram, T. H.; Tivanski, A. V.; Stone, E. A.; Prather, K. A.; Grassian, V. H. Molecular Diversity of Sea Spray Aerosol Particles: Impact of Ocean Biology on Particle Composition and Hygroscopicity. *Chem* **2017**, *2*, 655−667.

(4) Prather, K. A.; Bertram, T. H.; Grassian, V. H.; Deane, G. B.; Stokes, M. D.; DeMott, P. J.; Aluwihare, L. I.; Palenik, B. P.; Azam, F.; Seinfeld, J. H.; Moffet, R. C.; Molina, M. J.; Cappa, C. D.; Geiger, F. M.; Roberts, G. C.; Russell, L. M.; Ault, A. P.; Baltrusaitis, J.; Collins, D. B.; Corrigan, C. E.; Cuadra-Rodriguez, L. A.; Ebben, C. J.; Forestieri, S. D.; Guasco, T. L.; Hersey, S. P.; Kim, M. J.; Lambert, W. F.; Modini, R. L.; Mui, W.; Pedler, B. E.; Ruppel, M. J.; Ryder, O. S.; Schoepp, N. G.; Sullivan, R. C.; Zhao, D. Bringing the ocean into the laboratory to probe the chemical complexity of sea spray aerosol. *Proc. Natl. Acad. Sci. U.S.A.* **2013**, *110*, 7550−7555.

(5) Sauer, J. M. K.; Lee, C.; Alves, M.; Amiri, S.; Bahaveolos, C.; Barnes, E.; Crocker, D.; Dinasquaet, J.; Garofalo, L.; Kaluarachchi, C.; Dang, D.; Kilgour, D.; Mael, L.; Mitts, B.; Moon, D.; Morris, C.; Moore, A.; Ni, C.-m.; Pendergraft, M.; Petras, D.; Simpson, R.; Smith, S.; Tumminello, P.; Walker, J.; Demott, P.; Farmer, D.; Goldstein, A.; Grassian, V.; Jaffe, J.; Malfatti, F.; Martz, T.; Slade, J.; Tivanski, A.; Bertram, T.; Cappa, C.; Prather, K. The Sea Spray Chemistry and Particle Evolution Study (SeaSCAPE): Overview and Experimental Methods. **2021**, chemrxiv:2021-sm7vw, This content is a preprint and has not been peer-reviewed.

(6) DeMott, P. J.; Hill, T. C. J.; McCluskey, C. S.; Prather, K. A.; Collins, D. B.; Sullivan, R. C.; Ruppel, M. J.; Mason, R. H.; Irish, V.

E.; Lee, T.; Hwang, C. Y.; Rhee, T. S.; Snider, J. R.; McMeeking, G. R.; Dhaniyala, S.; Lewis, E. R.; Wentzell, J. J. B.; Abbatt, J.; Lee, C.; Sultana, C. M.; Ault, A. P.; Axson, J. L.; Diaz Martinez, M.; Venero, I.; Santos-Figueroa, G.; Stokes, M. D.; Deane, G. B.; Mayol-Bracero, O. L.; Grassian, V. H.; Bertram, T. H.; Bertram, A. K.; Moffett, B. F.; Franc, G. D. Sea spray aerosol as a unique source of ice nucleating particles. *Proc. Natl. Acad. Sci. U.S.A.* **2016**, *113*, 5797−5803.

(7) DeMott, P. J.; Hill, T. C. J.; Petters, M. D.; Bertram, A. K.; Tobo, Y.; Mason, R. H.; Suski, K. J.; McCluskey, C. S.; Levin, E. J. T.; Schill, G. P.; Boose, Y.; Rauker, A. M.; Miller, A. J.; Zaragoza, J.; Rocci, K.; Rothfuss, N. E.; Taylor, H. P.; Hader, J. D.; Chou, C.; Huffman, J. A.; Pöschl, U.; Prenni, A. J.; Kreidenweis, S. M. Comparative measurements of ambient atmospheric concentrations of ice nucleating particles using multiple immersion freezing methods and a continuous flow diffusion chamber. *Atmos. Chem. Phys.* **2017**, *17*, 11227−11245.

(8) Schill, S. R.; Collins, D. B.; Lee, C.; Morris, H. S.; Novak, G. A.; Prather, K. A.; Quinn, P. K.; Sultana, C. M.; Tivanski, A. V.; Zimmermann, K.; Cappa, C. D.; Bertram, T. H. The Impact of Aerosol Particle Mixing State on the Hygroscopicity of Sea Spray Aerosol. *ACS Cent. Sci.* **2015**, *1*, 132−141.

(9) Morris, H. S.; Estillore, A. D.; Laskina, O.; Grassian, V. H.; Tivanski, A. V. Quantifying the Hygroscopic Growth of Individual Submicrometer Particles with Atomic Force Microscopy. *Anal. Chem.* **2016**, *88*, 3647−3654.

(10) Lee, H. D.; Wigley, S.; Lee, C.; Or, V. W.; Hasenecz, E. S.; Stone, E. A.; Grassian, V. H.; Prather, K. A.; Tivanski, A. V. Physicochemical Mixing State of Sea Spray Aerosols: Morphologies Exhibit Size Dependence. *Acs Earth Space Chem.* **2020**, *4*, 1604−1611.

(11) Sellegri, K.; O'Dowd, C. D.; Yoon, Y. J.; Jennings, S. G.; de Leeuw, G. Surfactants and submicron sea spray generation. *J. Geophys. Res.: Atmos.* **2006**, *111*, D22215.

(12) DeMott, P. J.; Prenni, A. J.; Liu, X.; Kreidenweis, S. M.; Petters, M. D.; Twohy, C. H.; Richardson, M. S.; Eidhammer, T.; Rogers, D. C. Predicting global atmospheric ice nuclei distributions and their impacts on climate. *Proc. Natl. Acad. Sci. U.S.A.* **2010**, *107*, 11217−11222.

(13) Simpson, W. R.; Brown, S. S.; Saiz-Lopez, A.; Thornton, J. A.; von Glasow, R. Tropospheric Halogen Chemistry: Sources, Cycling, and Impacts. *Chem. Rev.* **2015**, *115*, 4035−4062.

(14) Abbatt, J. P. D.; Lee, A. K. Y.; Thornton, J. A. Quantifying trace gas uptake to tropospheric aerosol: recent advances and remaining challenges. *Chem. Soc. Rev.* **2012**, *41*, 6555−6581.

(15) Shiraiwa, M.; Ammann, M.; Koop, T.; Poschl, U. Gas uptake and chemical aging of semisolid organic aerosol particles. *Proc. Natl. Acad. Sci. U.S.A.* **2011**, *108*, 11003−11008.

(16) Cochran, R. E.; Laskina, O.; Jayarathne, T.; Laskin, A.; Laskin, J.; Lin, P.; Sultana, C.; Lee, C.; Moore, K. A.; Cappa, C. D.; Bertram, T. H.; Prather, K. A.; Grassian, V. H.; Stone, E. A. Analysis of Organic Anionic Surfactants in Fine and Coarse Fractions of Freshly Emitted Sea Spray Aerosol. *Environ. Sci. Technol.* **2016**, *50*, 2477−2486.

(17) Cochran, R. E.; Jayarathne, T.; Stone, E. A.; Grassian, V. H. Selectivity Across the Interface: A Test of Surface Activity in the Composition of Organic-Enriched Aerosols from Bubble Bursting. *J. Phys. Chem. Lett.* **2016**, *7*, 1692−1696.

(18) Engel, A.; Sperling, M.; Sun, C. C.; Grosse, J.; Friedrichs, G. Organic Matter in the Surface Microlayer: Insights From a Wind Wave Channel Experiment. *Front. Mar. Sci.* **2018**, *5*, 185.

(19) Facchini, M. C.; Rinaldi, M.; Decesari, S.; Carbone, C.; Finessi, E.; Mircea, M.; Fuzzi, S.; Ceburnis, D.; Flanagan, R.; Nilsson, E. D.; de Leeuw, G.; Martino, M.; Woeltjen, J.; O'Dowd, C. D. Primary submicron marine aerosol dominated by insoluble organic colloids and aggregates. *Geophys. Res. Lett.* **2008**, *35*, L17814.

(20) Schill, S. R.; Burrows, S. M.; Hasenecz, E. S.; Stone, E. A.; Bertram, T. H. The Impact of Divalent Cations on the Enrichment of Soluble Saccharides in Primary Sea Spray Aerosol. *Atmosphere* **2018**, *9*, 476.

(21) Wang, X.; Deane, G. B.; Moore, K. A.; Ryder, O. S.; Stokes, M. D.; Beall, C. M.; Collins, D. B.; Santander, M. V.; Burrows, S. M.; Sultana, C. M.; Prather, K. A. The role of jet and film drops in controlling the mixing state of submicron sea spray aerosol particles. *Proc. Natl. Acad. Sci. U.S.A.* **2017**, *114*, 6978−6983.

(22) Kaluarachchi, C. P.; Lee, H. D.; Lan, Y.; Lansakara, T. I.; Tivanski, A. V. Surface Tension Measurements of Aqueous Liquid−Air Interfaces Probed with Microscopic Indentation. *Langmuir* **2021**, *37*, 2457.

(23) Wang, X.; Sultana, C. M.; Trueblood, J.; Hill, T. C. J.; Malfatti, F.; Lee, C.; Laskina, O.; Moore, K. A.; Beall, C. M.; McCluskey, C. S.; Cornwell, G. C.; Zhou, Y.; Cox, J. L.; Pendergraft, M. A.; Santander, M. V.; Bertram, T. H.; Cappa, C. D.; Azam, F.; DeMott, P. J.; Grassian, V. H.; Prather, K. A. Microbial Control of Sea Spray Aerosol Composition: A Tale of Two Blooms. *ACS Cent. Sci.* **2015**, *1*, 124−131.

(24) Lv, C.; Tsona, N. T.; Du, L. Sea spray aerosol formation: Results on the role of different parameters and organic concentrations from bubble bursting experiments. *Chemosphere* **2020**, *252*, 126456.

(25) Jayarathne, T.; Sultana, C. M.; Lee, C.; Malfatti, F.; Cox, J. L.; Pendergraft, M. A.; Moore, K. A.; Azam, F.; Tivanski, A. V.; Cappa, C. D.; Bertram, T. H.; Grassian, V. H.; Prather, K. A.; Stone, E. A. Enrichment of Saccharides and Divalent Cations in Sea Spray Aerosol During Two Phytoplankton Blooms. *Environ. Sci. Technol.* **2016**, *50*, 11511−11520.

(26) Ault, A. P.; Moffet, R. C.; Baltrusaitis, J.; Collins, D. B.; Ruppel, M. J.; Cuadra-Rodriguez, L. A.; Zhao, D.; Guasco, T. L.; Ebben, C. J.; Geiger, F. M.; Bertram, T. H.; Prather, K. A.; Grassian, V. H. Size-Dependent Changes in Sea Spray Aerosol Composition and Properties with Different Seawater Conditions. *Environ. Sci. Technol.* **2013**, *47*, 5603−5612.

(27) Crocker, D. R.; Hernandez, R. E.; Huang, H. D.; Pendergraft, M. A.; Cao, R.; Dai, J.; Morris, C. K.; Deane, G. B.; Prather, K. A.; Thiemens, M. H. Biological Influence on δ13C and Organic Composition of Nascent Sea Spray Aerosol. *Acs Earth Space Chem.* **2020**, *4*, 1686−1699.

(28) Cavalli, F.; Facchini, M. C.; Decesari, S.; Mircea, M.; Emblico, L.; Fuzzi, S.; Ceburnis, D.; Yoon, Y. J.; O'Dowd, C. D.; Putaud, J. P.; Dell'Acqua, A. Advances in characterization of size-resolved organic matter in marine aerosol over the North Atlantic. *J. Geophys. Res.: Atmos.* **2004**, *109*, D24215.

(29) Quinn, P. K.; Bates, T. S.; Schulz, K. S.; Coffman, D. J.; Frossard, A. A.; Russell, L. M.; Keene, W. C.; Kieber, D. J. Contribution of sea surface carbon pool to organic matter enrichment in sea spray aerosol. *Nat. Geosci.* **2014**, *7*, 228−232.

(30) Cunliffe, M.; Engel, A.; Frka, S.; Gašparović, B.; Guitart, C.; Murrell, J. C.; Salter, M.; Stolle, C.; Upstill-Goddard, R.; Wurl, O. Sea surface microlayers: A unified physicochemical and biological perspective of the air-ocean interface. *Prog. Oceanogr.* **2013**, *109*, 104−116.

(31) Cochran, R. E.; Ryder, O. S.; Grassian, V. H.; Prather, K. A. Sea Spray Aerosol: The Chemical Link between the Oceans, Atmosphere, and Climate. *Acc. Chem. Res.* **2017**, *50*, 599−604.

(32) Hasenecz, E. S.; Jayarathne, T.; Pendergraft, M. A.; Santander, M. V.; Mayer, K. J.; Sauer, J.; Lee, C.; Gibson, W. S.; Kruse, S. M.; Malfatti, F.; Prather, K. A.; Stone, E. A. Marine Bacteria Affect Saccharide Enrichment in Sea Spray Aerosol during a Phytoplankton Bloom. *Acs Earth Space Chem.* **2020**, *4*, 1638−1649.

(33) Li, W.; Shao, L.; Zhang, D.; Ro, C.-U.; Hu, M.; Bi, X.; Geng, H.; Matsuki, A.; Niu, H.; Chen, J. A review of single aerosol particle studies in the atmosphere of East Asia: morphology, mixing state, source, and heterogeneous reactions. *J. Cleaner Prod.* **2016**, *112*, 1330−1349.

(34) Riemer, N.; Ault, A. P.; West, M.; Craig, R. L.; Curtis, J. H. Aerosol Mixing State: Measurements, Modeling, and Impacts. *Rev. Geophys.* **2019**, *57*, 187−249.

(35) Estillore, A. D.; Morris, H. S.; Or, V. W.; Lee, H. D.; Alves, M. R.; Marciano, M. A.; Laskina, O.; Qin, Z.; Tivanski, A. V.; Grassian, V. H. Linking hygroscopicity and the surface microstructure of model inorganic salts, simple and complex carbohydrates, and authentic sea spray aerosol particles. *Phys. Chem. Chem. Phys.* **2017**, *19*, 21101−21111.

(36) Morris, H. S.; Grassian, V. H.; Tivanski, A. V. Correction: Humidity-dependent surface tension measurements of individual inorganic and organic submicrometre liquid particles. *Chem. Sci.* **2015**, *6*, 6021.

(37) Zhang, Y.; Chen, Y.; Lambe, A. T.; Olson, N. E.; Lei, Z.; Craig, R. L.; Zhang, Z.; Gold, A.; Onasch, T. B.; Jayne, J. T.; Worsnop, D. R.; Gaston, C. J.; Thornton, J. A.; Vizuete, W.; Ault, A. P.; Surratt, J. D. Effect of the Aerosol-Phase State on Secondary Organic Aerosol Formation from the Reactive Uptake of Isoprene-Derived Epoxydiols (IEPOX). *Environ. Sci. Technol. Lett.* **2018**, *5*, 167−174.

(38) Ray, K. K.; Lee, H. D.; Gutierrez, M. A.; Chang, F. J.; Tivanski, A. V. Correlating 3D Morphology, Phase State, and Viscoelastic Properties of Individual Substrate-Deposited Particles. *Anal. Chem.* **2019**, *91*, 7621−7630.

(39) Ault, A. P.; Axson, J. L. Atmospheric Aerosol Chemistry: Spectroscopic and Microscopic Advances. *Anal. Chem.* **2017**, *89*, 430−452.

(40) Laskina, O.; Morris, H. S.; Grandquist, J. R.; Qin, Z.; Stone, E. A.; Tivanski, A. V.; Grassian, V. H. Size Matters in the Water Uptake and Hygroscopic Growth of Atmospherically Relevant Multicomponent Aerosol Particles. *J. Phys. Chem. A* **2015**, *119*, 4489−4497.

(41) Lee, H. D.; Estillore, A. D.; Morris, H. S.; Ray, K. K.; Alejandro, A.; Grassian, V. H.; Tivanski, A. V. Direct Surface Tension Measurements of Individual Sub-Micrometer Particles Using Atomic Force Microscopy. *J. Phys. Chem. A* **2017**, *121*, 8296−8305.

(42) Lee, H. D.; Ray, K. K.; Tivanski, A. V. Solid, Semisolid, and Liquid Phase States of Individual Submicrometer Particles Directly Probed Using Atomic Force Microscopy. *Anal. Chem.* **2017**, *89*, 12720−12726.

(43) Shiraiwa, M.; Zuend, A.; Bertram, A. K.; Seinfeld, J. H. Gas-particle partitioning of atmospheric aerosols: interplay of physical state, non-ideal mixing and morphology. *Phys. Chem. Chem. Phys.* **2013**, *15*, 11441−11453.

(44) You, Y.; Renbaum-Wolff, L.; Carreras-Sospedra, M.; Hanna, S. J.; Hiranuma, N.; Kamal, S.; Smith, M. L.; Zhang, X.; Weber, R. J.; Shilling, J. E.; Dabdub, D.; Martin, S. T.; Bertram, A. K. Images reveal that atmospheric particles can undergo liquid-liquid phase separations. *Proc. Natl. Acad. Sci. U.S.A.* **2012**, *109*, 13188−13193.

(45) Hodas, N.; Zuend, A.; Mui, W.; Flagan, R. C.; Seinfeld, J. H. Influence of particle-phase state on the hygroscopic behavior of mixed organic-inorganic aerosols. *Atmos. Chem. Phys.* **2015**, *15*, 5027−5045.

(46) Murray, B. J. Inhibition of ice crystallisation in highly viscous aqueous organic acid droplets. *Atmos. Chem. Phys.* **2008**, *8*, 5423−5433.

(47) Murray, B. J.; Wilson, T. W.; Dobbie, S.; Cui, Z.; Al-Jumur, S. M. R. K.; Möhler, O.; Schnaiter, M.; Wagner, R.; Benz, S.; Niemand, M.; Saathoff, H.; Ebert, V.; Wagner, S.; Kärcher, B. Heterogeneous nucleation of ice particles on glassy aerosols under cirrus conditions. *Nat. Geosci.* **2010**, *3*, 233−237.

(48) Kuwata, M.; Martin, S. T. Particle Size Distributions following Condensational Growth in Continuous Flow Aerosol Reactors as Derived from Residence Time Distributions: Theoretical Development and Application to Secondary Organic Aerosol. *Aerosol Sci. Technol.* **2012**, *46*, 937−949.

(49) Song, Y. C.; Haddrell, A. E.; Bzdek, B. R.; Reid, J. P.; Bannan, T.; Topping, D. O.; Percival, C.; Cai, C. Measurements and Predictions of Binary Component Aerosol Particle Viscosity. *J. Phys. Chem. A* **2016**, *120*, 8123−8137.

(50) Pham, D. Q.; O'Brien, R.; Fraund, M.; Bonanno, D.; Laskina, O.; Beall, C.; Moore, K. A.; Forestieri, S.; Wang, X.; Lee, C.; Sultana, C.; Grassian, V.; Cappa, C. D.; Prather, K. A.; Moffet, R. C. Biological Impacts on Carbon Speciation and Morphology of Sea Spray Aerosol. *ACS Earth Space Chem.* **2017**, *1*, 551−561.

(51) Berkemeier, T.; Steimer, S. S.; Krieger, U. K.; Peter, T.; Pöschl, U.; Ammann, M.; Shiraiwa, M. Ozone uptake on glassy, semi-solid and liquid organic matter and the role of reactive oxygen intermediates in atmospheric aerosol chemistry. *Phys. Chem. Chem. Phys.* **2016**, *18*, 12662−12674.

(52) Koop, T.; Bookhold, J.; Shiraiwa, M.; Pöschl, U. Glass transition and phase state of organic compounds: dependency on molecular properties and implications for secondary organic aerosols in the atmosphere. *Phys. Chem. Chem. Phys.* **2011**, *13*, 19238−19255.

(53) Shiraiwa, M.; Berkemeier, T.; Schilling-Fahnestock, K. A.; Seinfeld, J. H.; Pöschl, U. Molecular corridors and kinetic regimes in the multiphase chemical evolution of secondary organic aerosol. *Atmos. Chem. Phys.* **2014**, *14*, 8323−8341.

(54) Wang, B. B.; Laskin, A.; Roedel, T.; Gilles, M. K.; Moffet, R. C.; Tivanski, A. V.; Knopf, D. A. Heterogeneous ice nucleation and water uptake by field-collected atmospheric particles below 273 K. *J. Geophys. Res.: Atmos.* **2012**, *117*, D00V19.

(55) Lee, H.; Kaluarachchi, C.; Hasenecz, S. E.; Zhu, J. Z.; Popa, E.; Stone, A. E.; Tivanski, A. Effect of dry or wet substrate deposition on the organic volume fraction of core-shell aerosol particles. *Atmos. Meas. Tech. Discuss.* **2018**, *12* (3), 2033−2042.

(56) Ryder, O. S.; Campbell, N. R.; Morris, H.; Forestieri, S.; Ruppel, M. J.; Cappa, C.; Tivanski, A.; Prather, K.; Bertram, T. H. Role of Organic Coatings in Regulating N_2O_5 Reactive Uptake to Sea Spray Aerosol. *J. Phys. Chem. A* **2015**, *119*, 11683−11692.

(57) Gupta, A.; Rawlings, J. B. Comparison of parameter estimation methods in stochastic chemical kinetic models: Examples in systems biology. *AIChE J.* **2014**, *60*, 1253−1268.

(58) van Ravenzwaaij, D.; Cassey, P.; Brown, S. D. A simple introduction to Markov Chain Monte−Carlo sampling. *Psychon. Bull. Rev.* **2018**, *25*, 143−154.

(59) Cappa, C. D.; Asadi, S.; Barreda, S.; Wexler, A. S.; Bouvier, N. M.; Ristenpart, W. D. Expiratory aerosol particle escape from surgical masks due to imperfect sealing. *Sci. Rep.* **2021**, *11*, 12110.

(60) Cappa, C. D.; Ristenpart, W. D.; Barreda, S.; Bouvier, N. M.; Levintal, E.; Wexler, A. S.; Roman, S. A. A highly efficient cloth facemask design. *Aerosol Sci. Technol.* **2021**, 1−17.

(61) Schauer, J. J.; Mader, B. T.; DeMinter, J. T.; Heidemann, G.; Bae, M. S.; Seinfeld, J. H.; Flagan, R. C.; Cary, R. A.; Smith, D.; Huebert, B. J.; Bertram, T.; Howell, S.; Kline, J. T.; Quinn, P.; Bates, T.; Turpin, B.; Lim, H. J.; Yu, J. Z.; Yang, H.; Keywood, M. D. ACE-Asia Intercomparison of a Thermal-Optical Method for the Determination of Particle-Phase Organic and Elemental Carbon. *Environ. Sci. Technol.* **2003**, 37 (5), 993−1001.

(62) Jayarathne, T.; Stockwell, C. E.; Yokelson, R. J.; Nakao, S.; Stone, E. A. Emissions of Fine Particle Fluoride from Biomass Burning. *Environ. Sci. Technol.* **2014**, *48*, 12636−12644.

(63) Holland, H. D. *The Chemistry of the Atmosphere and Oceans*; Wiley: New York, 1978.

(64) Mitts, B. A.; Wang, X. F.; Lucero, D. D.; Beall, C. M.; Deane, G. B.; DeMott, P. J.; Prather, K. A. Importance of Supermicron Ice Nucleating Particles in Nascent Sea Spray. *Geophys. Res. Lett.* **2021**, *48*, No. e2020GL089633.

(65) Alpert, P. A.; Kilthau, W. P.; Bothe, D. W.; Radway, J. C.; Aller, J. Y.; Knopf, D. A. The influence of marine microbial activities on aerosol production: A laboratory mesocosm study. *J. Geophys. Res.: Atmos.* **2015**, *120*, 8841−8860.

(66) Aller, J. Y.; Radway, J. C.; Kilthau, W. P.; Bothe, D. W.; Wilson, T. W.; Vaillancourt, R. D.; Quinn, P. K.; Coffman, D. J.; Murray, B. J.; Knopf, D. A. Size-resolved characterization of the polysaccharidic and proteinaceous components of sea spray aerosol. *Atmos. Environ.* **2017**, *154*, 331−347.

(67) O'Dowd, C. D.; Facchini, M. C.; Cavalli, F.; Ceburnis, D.; Mircea, M.; Decesari, S.; Fuzzi, S.; Yoon, Y. J.; Putaud, J.-P. Biogenically driven organic contribution to marine aerosol. *Nature* **2004**, *431*, 676−680.

(68) O'Dowd, C. D.; Scannell, C. A Global Emission Inventory of Submicron Sea-spray Aerosols. In *Nucleation and Atmospheric Aerosols*; O'Dowd, C. D., Wagner, P. E., Eds.; Springer Netherlands: Dordrecht, 2007; pp 1079−1082.

(69) Collins, D. B.; Zhao, D. F.; Ruppel, M. J.; Laskina, O.; Grandquist, J. R.; Modini, R. L.; Stokes, M. D.; Russell, L. M.; Bertram, T. H.; Grassian, V. H.; Deane, G. B.; Prather, K. A. Direct aerosol chemical composition measurements to evaluate the

physicochemical differences between controlled sea spray aerosol generation schemes. *Atmos. Meas. Tech.* **2014**, *7*, 3667−3683.

(70) Bates, T. S.; Quinn, P. K.; Frossard, A. A.; Russell, L. M.; Hakala, J.; Petaja, T.; Kulmala, M.; Covert, D. S.; Cappa, C. D.; Li, S. M.; Hayden, K. L.; Nuaaman, I.; McLaren, R.; Massoli, P.; Canagaratna, M. R.; Onasch, T. B.; Sueper, D.; Worsnop, D. R.; Keene, W. C. Measurements of ocean derived aerosol off the coast of California. *J. Geophys. Res.: Atmos.* **2012**, *117*, D00V15.

(71) Lee, H. D.; Wigley, S.; Lee, C.; Or, V. W.; Hasenecz, E. S.; Stone, E. A.; Grassian, V. H.; Prather, K. A.; Tivanski, A. V. Physicochemical Mixing State of Sea Spray Aerosols: Morphologies Exhibit Size Dependence. *ACS Earth Space Chem.* **2020**, *4*, 1604.

(72) Bar, G.; Thomann, Y.; Brandsch, R.; Cantow, H.-J.; Whangbo, M.-H. Factors affecting the height and phase images in tapping mode atomic force microscopy. Study of phase-separated polymer blends of poly(ethene-co-styrene) and poly(2,6-dimethyl-1,4-phenylene oxide). *Langmuir* **1997**, *13*, 3807−3812.

(73) Parikh, S. J.; Chorover, J. Infrared spectroscopy studies of cation effects on lipopolysaccharides in aqueous solution. *Colloids Surf., B* **2007**, *55*, 241−250.

(74) Çaykara, T.; Demirci, S.; Eroğlu, M. S.; Güven, O. Poly(ethylene oxide) and its blends with sodium alginate. *Polymer* **2005**, *46*, 10750−10757.

(75) Wiercigroch, E.; Szafraniec, E.; Czamara, K.; Pacia, M. Z.; Majzner, K.; Kochan, K.; Kaczor, A.; Baranska, M.; Malek, K. Raman and infrared spectroscopy of carbohydrates: A review. *Spectrochim. Acta, Part A* **2017**, *185*, 317−335.

(76) Papageorgiou, S. K.; Kouvelos, E. P.; Favvas, E. P.; Sapalidis, A. A.; Romanos, G. E.; Katsaros, F. K. Metal−carboxylate interactions in metal−alginate complexes studied with FTIR spectroscopy. *Carbohydr. Res.* **2010**, *345*, 469−473.

(77) Hasenecz, E. S.; Kaluarachchi, C. P.; Lee, H. D.; Tivanski, A. V.; Stone, E. A. Saccharide Transfer to Sea Spray Aerosol Enhanced by Surface Activity, Calcium, and Protein Interactions. *Acs Earth Space Chem.* **2019**, *3*, 2539−2548.

(78) Andreae, M. O.; Charlson, R. J.; Bruynseels, F.; Storms, H.; Van Grieken, R.; Maenhaut, W. Internal Mixture of Sea Salt, Silicates, and Excess Sulfate in Marine Aerosols. *Science* **1986**, *232*, 1620−1623.

(79) Maria, S. F.; Russell, L. M.; Turpin, B. J.; Porcja, R. J. FTIR measurements of functional groups and organic mass in aerosol samples over the Caribbean. *Atmos. Environ.* **2002**, *36*, 5185−5196.

(80) Yamamoto, M.; Sakurai, Y.; Hosoi, Y.; Ishii, H.; Kajikawa, K.; Ouchi, Y.; Seki, K. Structures of a long-chain n-alkane, n-C44H90, on a Au(111) surface: An infrared reflection absorption spectroscopic study. *J. Phys. Chem. B* **2000**, *104*, 7363−7369.

(81) Leu, M.-T.; Timonen, R. S.; Keyser, L. F.; Yung, Y. L. Heterogeneous Reactions of HNO3(g) + NaCl(s) .fwdarw. HCl(g) + NaNO3(s) and N2O5(g) + NaCl(s) .fwdarw. ClNO2(g) + NaNO3(s). *J. Phys. Chem.* **1995**, *99*, 13203−13212.

(82) Zangmeister, C. D.; Pemberton, J. E. Raman Spectroscopy of the Reaction of Sodium Chloride with Nitric Acid:Sodium Nitrate Growth and Effect of Water Exposure. *J. Phys. Chem. A* **2004**, *108*, 236.

(83) Nakamoto, K. Applications in Inorganic Chemistry. *Infrared and Raman Spectra of Inorganic and Coordination Compounds*; John Wiley & Sons, Inc., 2008; pp 149-354.

(84) Goebbert, D. J.; Garand, E.; Wende, T.; Bergmann, R.; Meijer, G.; Asmis, K. R.; Neumark, D. M. Infrared Spectroscopy of the Microhydrated Nitrate Ions NO3−(H2O)1−6. *J. Phys. Chem. A* **2009**, *113*, 7584−7592.

(85) Petters, M. D.; Kreidenweis, S. M. A single parameter representation of hygroscopic growth and cloud condensation nucleus activity. *Atmos. Chem. Phys.* **2007**, *7*, 1961−1971.

(86) Forestieri, S. D.; Cornwell, G. C.; Helgestad, T. M.; Moore, K. A.; Lee, C.; Novak, G. A.; Sultana, C. M.; Wang, X.; Bertram, T. H.; Prather, K. A.; Cappa, C. D. Linking variations in sea spray aerosol particle hygroscopicity to composition during two microcosm experiments. *Atmos. Chem. Phys.* **2016**, *16*, 9003−9018.

(87) Marshall, F. H.; Berkemeier, T.; Shiraiwa, M.; Nandy, L.; Ohm, P. B.; Dutcher, C. S.; Reid, J. P. Influence of particle viscosity on mass transfer and heterogeneous ozonolysis kinetics in aqueous-sucrose-maleic acid aerosol. *Phys. Chem. Chem. Phys.* **2018**, *20*, 15560−15573.

(88) Shiraiwa, M.; Li, Y.; Tsimpidi, A. P.; Karydis, V. A.; Berkemeier, T.; Pandis, S. N.; Lelieveld, J.; Koop, T.; Pöschl, U. Global distribution of particle phase state in atmospheric secondary organic aerosols. *Nat. Commun.* **2017**, *8*, 15002.